SCIENTIFIC REPORTS

Received: 7 March 2018
Accepted: 27 July 2018

Quantification of the ozone and singlet delta oxygen produced in gas and liquid phases by a non-thermal atmospheric plasma with relevance for medical treatment

Helena Jablonowski[1], Joao Santos Sousa[2], Klaus-Dieter Weltmann[3], Kristian Wende[1] & Stephan Reuter[3]

In the field of plasma medicine, the identification of relevant reactive species in the liquid phase is highly important. To design the plasma generated species composition for a targeted therapeutic application, the point of origin of those species needs to be known. The dominant reactive oxygen species generated by the plasma used in this study are atomic oxygen, ozone, and singlet delta oxygen. The species density changes with the distance to the active plasma zone, and, hence, the oxidizing potential of this species cocktail can be tuned by altering the treatment distance. In both phases (gas and liquid), independent techniques have been used to determine the species concentration as a function of the distance. The surrounding gas composition and ambient conditions were controlled between pure nitrogen and air-like by using a curtain gas device. In the gas phase, in contrast to the ozone density, the singlet delta oxygen density showed to be more sensitive to the distance. Additionally, by changing the surrounding gas, admixing or not molecular oxygen, the dynamics of ozone and singlet delta oxygen behave differently. Through an analysis of the reactive species development for the varied experimental parameters, the importance of several reaction pathways for the proceeding reactions was evaluated and some were eventually excluded.

Cold physical plasma jets have shown a high potential in the treatment of chronic wounds[1–3] and in cancer as an adjuvant to standard therapy[4]. Further targets are currently investigated, e.g. atopic eczema[5]. Common to all these applications is that reactive oxygen species (ROS) have relevant impact via redox signalling processes[6,7]. Besides electromagnetic radiation (ultraviolet - UV - up to near infrared - NIR - spectral range), atmospheric pressure plasma jets generate various reactive oxygen and reactive nitrogen species (RNS), such as ozone, singlet delta oxygen, hydroxyl radicals, superoxide anion radicals, nitric monoxide, nitrogen dioxide, nitrite, and nitrate[8]. Most of these species are thought to interact directly or indirectly with biological systems, e.g. cells in a human body. In order to tailor the plasma composition for a given medical application, it is essential to characterize the plasma, the reactive species deposited in liquids, and the subsequent biological effects of those reactive species. Hence, knowing the details of the transfer of the reactive species from the gas phase into liquids helps the interpretation of biological data and is useful to the construction of dedicated plasma sources. It also helps to evaluate the suitability of remote treatment approaches for medical usage that are being studied with increasing emphasis. Although increasing knowledge is available on time- and spatially resolved density distribution of reactive species in the gas phase, their trajectories in a liquid system remain elusive[8–11]. The formation pathway of many species in the liquids is not clear: liquid phase species can either be generated by a direct interaction of the plasma with the liquid at the interface[12], e.g. due to (vacuum)UV-caused photo dissociation of water molecules[13,14], or

[1]ZIK plasmatis at Leibniz Institute for Plasma Science and Technology e.V. (INP Greifswald e.V.), Felix-Hausdorff-Str. 2, 17489, Greifswald, Germany. [2]LPGP, CNRS, Univ. Paris-Sud, Université Paris-Saclay, 91405, Orsay, France. [3]Leibniz Institute for Plasma Science and Technology e.V. (INP Greifswald e.V.), Felix-Hausdorff-Str. 2, 17489, Greifswald, Germany. Kristian Wende and Stephan Reuter contributed equally to this work. Correspondence and requests for materials should be addressed to H.J. (email: helena.jablonowski@inp-greifswald.de)

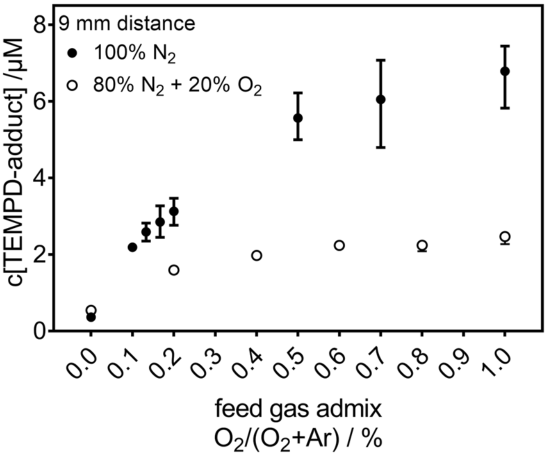

Figure 1. Concentration of spin probe TEMPD-HCl adducts after direct plasma treatment (9 mm, 180 s). In both environmental conditions (N_2 or air-like), plasma induces ROS in the liquid. The TEMPD-HCl adduct of O_3, $^\bullet O$, $O_2(a^1\Delta_g)$ is depicted as function of the O_2 content in the feed gas of Ar.

alternatively, via transfer from the gas phase into the liquid[15], or even by secondary or tertiary reactions in the bulk liquid[16]. One of the few species whose formation pathway in the liquids is well studied is hydrogen peroxide in the case of plasma jets fed with humidified argon[15,17] and helium[18] gases. Shortcomings in specificity or sensitivity limit bar the quantification of most other species in liquids. Short lifetimes or rapid conversions further impede quantification[19]. Some more recent approaches start to overcome these limits[12,19–22]. Models predict a large role of the interface layer, with impact on species attachment and solvation into the bulk liquid[12,23–27]. Yet, knowledge on the species distribution in the bulk liquid, especially when in contact with a biological surface or in presence of organic molecules, is very limited[23,24,28]. On the other hand, a large body of evidence exists, showing the impact of plasma derived species in biological systems, proving the permeation of the aqueous barriers, like physiologic buffer systems, cell culture media, or body fluids[10,11,29–36].

At times, specific plasma-generated species have been attributed to trigger the stimulation, modulation, or execution of the biological effects observed. Among these are hydrogen peroxide (H_2O_2)[15,17], atomic oxygen ($^\bullet O$)[37], or nitric oxide ($^\bullet NO$)[38] and peroxynitrite ($ONOO^-$)[16,22,39]. Other species are harder to pinpoint, although present in high amounts in the gas phase. This is valid for plasma generated ozone, O_3[40], and singlet delta oxygen, $O_2(a^1\Delta_g)$[41], whose full biological impact in plasma medicine is far from being completely known. O_3 is a powerful oxidant which is well known for disinfection of drinking water[42]. In this case, O_3 is the precursor for even stronger oxidants such as the hydroxyl radical ($^\bullet OH$)[43]. The lifetime of O_3 is relatively long; in water, O_3 has a half-life of seconds up to hours[44], depending on the temperature and the pH value[45]. Hence, in solution, the lifetime of O_3 is much longer than the half-life of $^\bullet OH$, which is of the order of ns[46]. In the gas phase, O_3 is even more stable; its half-life is in the range of hours up to days[47], depending on the temperature, humidity and air speed. $O_2(a^1\Delta_g)$ is also a highly reactive ROS. In comparison to O_3, it is less stable in both the gas and the liquid phases. Its half-life is 75 minutes in the gas phase[41] and several µs in the liquid phase[48]. Nevertheless, $O_2(a^1\Delta_g)$ is still more stable than most oxygen radicals. In the presence of superoxide anion radicals, $O_2^{\bullet -}$, $O_2(a^1\Delta_g)$ is quenched to molecular oxygen[49]. If H_2O_2 and hypochlorite (OCl^-) are simultaneously present in the solution, $O_2(a^1\Delta_g)$ can be generated directly in the liquid[50]. Biological effects of $O_2(a^1\Delta_g)$ are evident in the context of the photodynamic therapy[51].

In the gas phase, the variation of $O_2(a^1\Delta_g)$ and O_3 densities as a function of the O_2 admixture to the feed gas has already been shown for several plasma sources[41,52–55]. Here, the $O_2(a^1\Delta_g)$ as well as the O_3 concentrations are determined, for the first time, in the liquid and in the gas phase under identical conditions. To study the origin and transfer between the gas and liquid phases of plasma generated O_3 and $O_2(a^1\Delta_g)$, a well-characterized argon plasma jet was used (kinpen09)[17,20,56,57]. By using a curtain gas device, the ambient conditions were controlled[58], allowing the modulation of the gas composition around the plasma plume. The O_2 content of the working gas was also regulated. This approach allows tuning the reactive species composition in the solution and increases the treatments reproducibility[17,59–61], forming the base for the presented data. The final aim of the present paper is to estimate the potential biological impact of these two ROS, O_3 and $O_2(a^1\Delta_g)$, and to evaluate the suitability of direct and indirect treatment procedures.

Results

Reactive oxygen species in the liquid. During the plasma treatment of DPBS (Dulbecco's phosphate buffered saline solution), several reactive oxygen species are induced in the liquid[10]: O_3, $^\bullet O$, or $O_2(a^1\Delta_g)$.

In Fig. 1, the concentration of the spin probe TEMPD-HCl adducts is given as a function of the O_2 content in the feed gas for two different curtain gas conditions (pure N_2 and synthetic air). This spin probe adduct is formed by a reaction with either O_3, $^\bullet O$, or $O_2(a^1\Delta_g)$. The composition of the gas surrounding the plasma plume influences the spin probe adduct concentration. Air-like conditions lead to a lower adduct-concentration than the pure N_2 curtain gas. Furthermore, the presence of O_2 in the surrounding yields a saturation of the adduct concentration for O_2 contents in the argon higher than 0.4%. For a curtain gas of N_2, there is always an increase of the adduct concentration, but at a lower rate for higher O_2 content in the feed gas – no clear saturation is observed. As

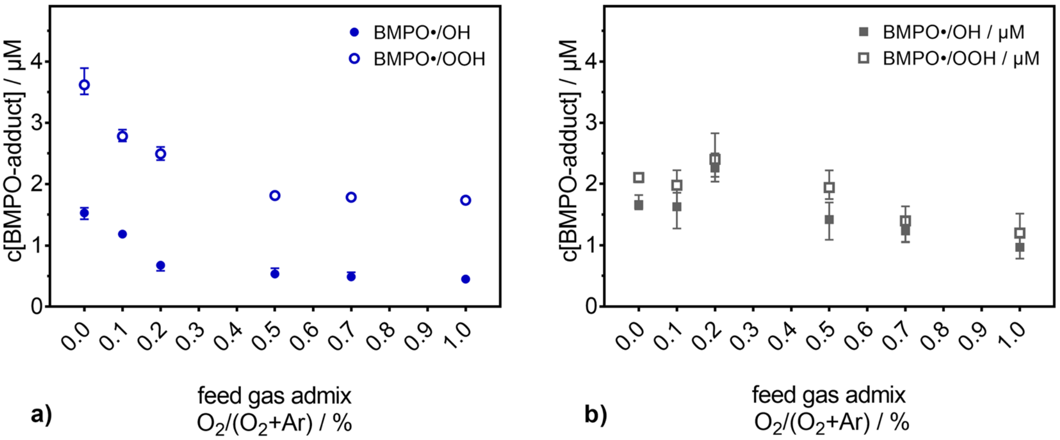

Figure 2. Concentration of free oxygen radical spin trap (BMPO) adducts after direct plasma treatment (9 mm, 180 s). The formation of the $^{\bullet}OH$ (filled symbols) and $O_2^{\bullet-}$ (open symbols) adducts is investigated as a function of the O_2 content in the feed gas of Ar under (**a**) pure N_2 or (**b**) air-like atmospheres.

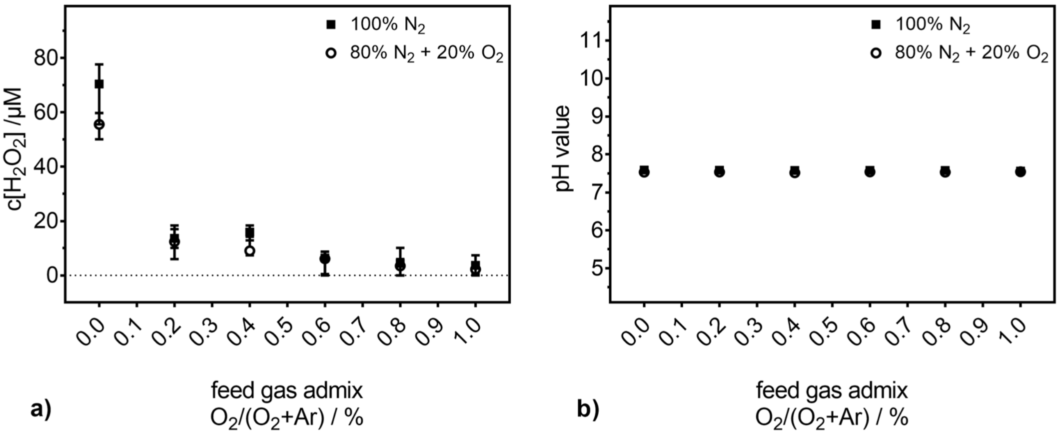

Figure 3. (**a**) H_2O_2 concentration and (**b**) stability of the pH value after direct plasma treatment (9 mm, 180 s). The values are depicted as a function of the O_2 content in the feed gas of Ar under N_2 or air-like atmospheres.

this spin probe results in the same EPR spectrum for the three potential reactants (O_3, $^{\bullet}O$, or $O_2(a^1\Delta_g)$), further measurements are necessary in order to distinguish the species and identify their origin.

The behaviour of $^{\bullet}OH$ and $O_2^{\bullet-}$ for similar experimental conditions was also studied. Using BMPO, $^{\bullet}OH$ and $O_2^{\bullet-}$ were detected for pure N_2 as curtain gas (see Fig. 2a) and an air-like atmosphere (see Fig. 2b). The resulting spin trap adducts, BMPO-OH and BMPO-OOH respectively, show an entirely different behaviour compared to the TEMPD-HCl adduct. However, the concentrations of both BMPO adducts have the same trend. For pure N_2 as curtain gas, their concentrations decrease with increasing O_2 content in the feed gas, and the strongest impact on the formation of the BMPO adducts occurs for low amounts of O_2: pure argon yields the highest concentration of BMPO adducts, which decreases drastically with the addition of 0.2% of O_2 or more. For an air-like atmosphere, the variation of the concentration of BMPO adducts as a function of the O_2 admixture into the feed gas is not so pronounced, with maxima concentrations being obtained for 0.2% of O_2 and the lowest concentrations for the higher O_2 content.

$^{\bullet}OH$ recombines in a diffusion-controlled manner to H_2O_2. Moreover, $O_2^{\bullet-}$ can also disproportionate to H_2O_2. Therefore, the H_2O_2 concentration was determined for the two curtain gas compositions. In Fig. 3a, the concentration of H_2O_2 in the liquid is given as a function of the O_2 content in the feed gas. A similar trend to those of the concentrations of $^{\bullet}OH$ and $O_2^{\bullet-}$ radicals was observed (if one do not consider the first two points for an air-like atmosphere).

Even if the experiments were performed in buffered saline solutions, the pH value was monitored. In Fig. 3b, it is shown that the pH value is stable for all studied conditions, including the untreated controls (not shown).

In order to study the formation pathways of the species present in the liquid, measurements in the gas phase are necessary. $O_2(a^1\Delta_g)$ is one of the possible candidates responsible for the formation of the obtained spin probe TEMPD-HCl adducts. Its density can be determined in the gas phase. Its detection by optical emission spectroscopy in the NIR may be disturbed by background radiation resulting from argon emission from the plasma.

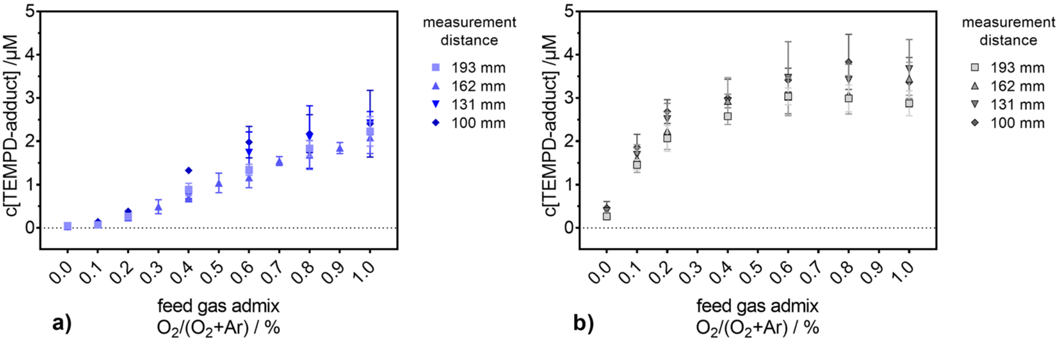

Figure 4. Concentration of spin probe adducts after indirect plasma treatment (d > 9 mm, 600 s). In pure N_2 (blue, (**a**)) as well as in air-like (gray, (**b**)) environments, the plasma induces ROS in the liquid for the various distances between the plasma jet's nozzle and the liquid studied (100, 131, 162, 193 mm).

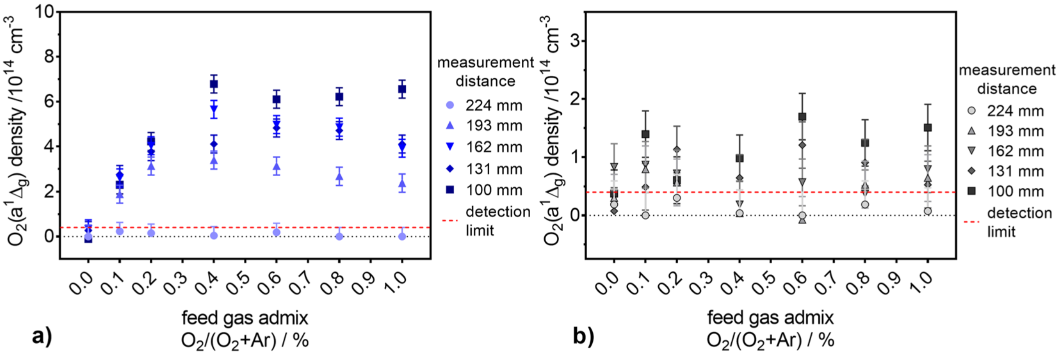

Figure 5. The $O_2(a^1\Delta_g)$ density in the plasma jet's exhaust for different measurement distances. The measurements were performed under pure N_2 (**a**) and air-like environments (**b**) for several amounts of O_2 in the feed gas. The $O_2(a^1\Delta_g)$ density detection limit of 4 10^{13} cm^{-3} is indicated by red dashed lines.

Therefore, a different experimental setup was used in order to reduce the argon emission reaching the detector (background noise). This was realized with a piece of bent glass connecting the plasma reactor and the measurement cell (see methods section for details), adversely limiting the shortest possible distance between the plasma jet's nozzle and the measurement point. Therefore, the species density in the gas phase can only be determined at distances of at least 100 mm from the nozzle of the kinpen09. Glass connectors with different lengths were used, and the TEMPD-HCl adduct measurements in the liquid phase were, thus, repeated for the different distances between the plasma jet's nozzle and the solutions. In Fig. 4, the obtained data is given in dependence of the O_2 content in the feed gas for both curtain gas compositions. As the treatment of the solutions was done by the guided gas exhaust of the plasma jet that passes through the measurement cell, the resulting concentration of TEMPD-HCl adduct was found to be below the detection limit if the treatment time was kept at 180 s, as in the direct plasma treatment. Therefore, the duration of the indirect plasma treatment was increased to 600 s, in order to reach sufficient adduct concentrations. The spin probe adduct concentrations obtained after indirect plasma treatment under pure N_2 or air-like atmosphere are given in Fig. 4a and 4b, respectively. Both conditions yield an increase of the concentration with increasing O_2 content in the feed gas. Although different trends were found for the two surrounding atmospheres, for each curtain gas the same trend is observed for all treatment distances. In contrast to the concentrations determined after direct plasma treatments at a distance of 9 mm (see Fig. 1), here, the higher concentrations were observed for an air-like curtain gas. Furthermore, for pure N_2 curtain gas, the concentrations of TEMPD-HCl adduct obtained after indirect plasma treatments are much lower than those gained after direct plasma treatments.

Reactive oxygen species in the gas phase. To gain further insight into the species generating the spin probe adducts, gas phase measurements were performed by calibrated infrared emission ($O_2(a^1\Delta_g)$) and UV-absorption spectroscopy (O_3). The dynamics of the $O_2(a^1\Delta_g)$ density in the gas phase was studied as a function of the O_2 content in the feed gas for different distances between the plasma jet's nozzle and the measurement cell (see Fig. 5a,b). The $O_2(a^1\Delta_g)$ density shows a clear dependence on the measurement distance; the shortest (100 mm) gap between the plasma jet's nozzle and the point of measurement yielded the highest measured densities for both curtain gases. With increasing distance, the densities become lower, and, at the longest distance (224 mm), only small amounts of $O_2(a^1\Delta_g)$ are still detectable (often below the limit of detection). Noise on low concentration points (below the limit of detection) at longer measurement distances resulted in slightly negative measurement values; these negative data points were zeroed.

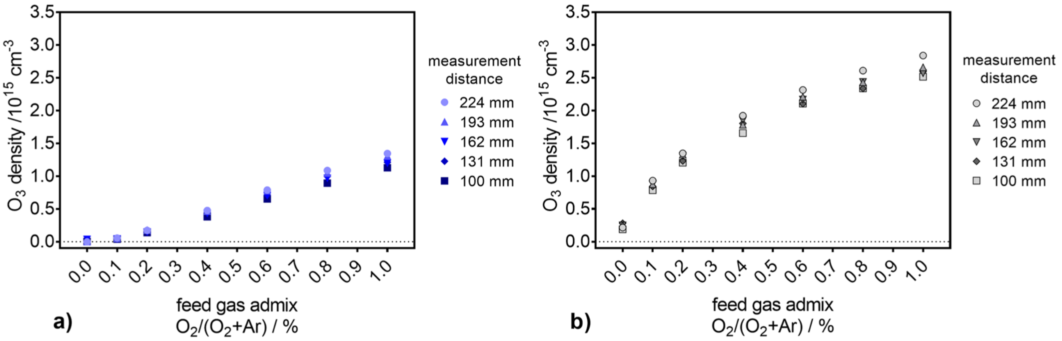

Figure 6. The O_3 density in the plasma jet's exhaust for different measurement distances. The measurements were performed under pure N_2 (blue, (**a**)) and air-like (gray, (**b**)) environments, for several amounts of O_2 in the feed gas.

In the case of N_2 as curtain gas (see Fig. 5a), the addition of O_2 yields a strong increase of the $O_2(a^1\Delta_g)$ gas phase density (noticeable for all distances but 224 mm, where the detected densities were in the range or below the detection limit and, as so, no clear statement can be given). As expected, when working with pure Ar feed gas surrounded by pure N_2 curtain gas, only traces of $O_2(a^1\Delta_g)$, in the range or below the detection limit, were detected regardless of the distance.

For an air-like curtain gas composition (see Fig. 5b), a clear, but less pronounced dependency of the $O_2(a^1\Delta_g)$ density on the distance between the plasma jet's nozzle and the measurement cell was also observed. In great contrast to the pure N_2 curtain condition, the O_2 content in the feed gas when surrounded by an air-like atmosphere seems to have no effect on the $O_2(a^1\Delta_g)$ gas phase density. Furthermore, the obtained $O_2(a^1\Delta_g)$ densities are lower here (maximum of $1.7\cdot10^{14}\,cm^{-3}$) compared to the N_2 curtain gas case (maximum of $6.75\cdot10^{14}\,cm^{-3}$).

In the gas phase measurements, O_3 behaves differently than $O_2(a^1\Delta_g)$: no distance dependency was observed for either gas curtain composition (see Fig. 6a,b). Moreover, the determined O_3 densities are an order of magnitude higher than those measured for $O_2(a^1\Delta_g)$. With increasing O_2 content in the feed gas, the O_3 density increases under both curtain gases, but a pure N_2 curtain gas yields lower O_3 densities (maximum of $1.25\cdot10^{15}\,cm^{-3}$), independently of the O_2 content in the feed gas. This is especially the case for the lower O_2 admixtures, where the slope of the increase of the O_3 density is lower when compared to the fast raise observed under the air-like curtain gas composition. Under this latter condition, the O_3 densities reached values of up to $2.5\cdot10^{15}\,cm^{-3}$. By comparing the maximal attained densities (obtained at 1% of O_2 admixture in the feed gas), one can state that the N_2 curtain gas yielded only half of the O_3 density generated in an air-like surrounding.

Discussion

During direct treatment of the liquid (DPBS) with the plasma plume (d = 9 mm, 180 s), a spin probe adduct of TEMPD-HCl can origin from a reaction with either O_3, $^\bullet O$ or $O_2(a^1\Delta_g)$, or a combination thereof. This adduct was measured for two different gas surroundings of the plasma plume (see Fig. 1). One of the compositions of the environment was a mixture of 80% of N_2 and 20% of O_2; the resulting adducts concentration increase as a function of the O_2 content in the feed gas, saturating for O_2 admixtures higher than 0.4%. The 100% N_2 gas curtain results in an even stronger increase of the adducts concentration, which starts to level out at high O_2 admixture but without reaching any saturation. It is known from literature that a pure N_2 surrounding prevents the quenching of $O_2(a^1\Delta_g)$, and, therefore, yields higher densities of $O_2(a^1\Delta_g)$ in the gas phase when O_2 is added to the feed gas[8]. In contrast, the presence of O_2 in the surrounding environment results in an increase of the O_3 gas density and in a decrease of the $O_2(a^1\Delta_g)$ gas density[8]. Assuming a direct solvation of $O_2(a^1\Delta_g)$ from the gas phase into the liquid, this predicted behaviour of the $O_2(a^1\Delta_g)$ gas density could directly explain the trends observed in the liquid for the TEMPD-HCl adducts (see Fig. 1). However, other reactive species, such as $^\bullet OH$, $O_2^{\bullet-}$, or H_2O_2, show a different response to the modified surrounding and the varied O_2 content in the feed gas, and $^\bullet OH$, $O_2^{\bullet-}$, and H_2O_2 can all contribute to the formation of at least $O_2(a^1\Delta_g)$, according to reactions 1 to 3[62–65].

$$O_2^{\bullet-} \rightarrow O_2\left(a^1\Delta_g\right) + e^- \tag{1}$$

$$O_2^{\bullet-} + {}^\bullet OH \rightarrow O_2\left(a^1\Delta_g\right) + OH^- \tag{2}$$

$$O_2^{\bullet-} + H_2O_2 \rightarrow O_2\left(a^1\Delta_g\right) + OH^- + {}^\bullet OH \tag{3}$$

In contrast to the TEMPD-HCl adducts (see Fig. 1), H_2O_2 deposition in the liquid does not strongly respond to changes in the composition of the curtain gas (see Fig. 3a). The H_2O_2 concentration was only slightly higher in a pure N_2 surrounding when no O_2 was admixed into the feed gas. If O_2 was present in the feed gas, the curtain gas composition did not influence the H_2O_2 concentration. Furthermore, H_2O_2, $^\bullet OH$, and $O_2^{\bullet-}$ behave similarly: with increasing O_2 content in the feed gas their resulting concentrations decrease in a pure N_2 surrounding. In fact, their close (chemical) relation to each other is well known[50]. $^\bullet OH$ and $O_2^{\bullet-}$ themselves do not yield to a paramagnetic product with TEMPD-HCl. This, together with the different behaviour, indicates that the $^{\bullet}OH$ and $O_2^{\bullet-}$ radicals as well as the H_2O_2 are not dominantly involved in the formation of O_3, $^{\bullet}O$, $O_2(a^1\Delta_g)$, and, therefore, they did not contribute to the measured TEMPD-HCl adduct. Additionally, as the pH value remained constant at 7.4 during all plasma treatments (see Fig. 3b), reactions containing the hydroperoxyl ($HO^{\bullet}_2$) radical can also be neglected: given its pK_a value of 4.8[50], only 0.25% of the $O_2^{\bullet-}$ radical is protonated. This means that $O_2^{\bullet-}$ concentrations in the μM range (concentration range measured for H_2O_2 – see Fig. 3a) result in a low nM $HO_2^{\bullet}$ concentration that can be diregarded.

Another possible mechanism of formation of $O_2(a^1\Delta_g)$ in aqueous solution is through OCl^-[11] (see equation 4). When the treated liquid contains chloride and the plasma source is producing $^{\bullet}O$ in the gas phase, these two species can react to form OCl^- [11,37]. Since the investigated solution, DPBS, contains chloride, this reaction cannot be excluded. Nevertheless, due to reaction 4, either H_2O_2 would be completely consumed in the solution by OCl^- or vice versa (depending on which species concentration is higher)[11]. The lifetime of $^{\bullet}O$, as a precursor for OCl^-, is quite short[9] in this plasma jet, so that only low OCl^- concentrations are expected to be formed. Furthermore, since H_2O_2 is still detectable (see Fig. 3a), it is assumed that H_2O_2 completely consumed OCl^-. Hence, the contribution of reaction 4 to the formation of $O_2(a^1\Delta_g)$ is expected to be negligible.

$$OCl^- + H_2O_2 \to HOCl + HO_2^- \to HOOCl + OH^- \to H_2O + ClOO^- \to O_2\left(a^1\Delta_g\right) + Cl^- \tag{4}$$

If $O_2(a^1\Delta_g)$ is excluded from being responsible for the spin probe adduct formation, O_3 is another potential candidate. O_3 is a major fraction of the plasma produced ROS in the gas phase, when conditions allow[8,23,40,66]. O_3 is not formed in the liquid; accordingly, it can only originate in the liquid phase through a solvation process from the gas phase.

A reaction of O_3 and H_2O_2 can occur, if both are simultaneously present in the liquid. The respective set of reactions is called peroxone process (see equations 5 to 7)[67,68]. Additional UV irradiation can enhance this process. Due to the bent glass connector present in the experimental setup used for indirect plasma treatments (see Fig. 8), the amount of UV radiation reaching the liquid, and available for this specific reaction is negligible. Therefore, the UV irradiation does not have a relevant impact compared to the other ongoing processes and reactions. Under acidic conditions, the peroxone process is relatively slow, but it becomes faster for neutral or alkaline pH. Hence, in DPBS with pH 7.4, this process may take place. As the $^{\bullet}OH$-adduct of BMPO and the H_2O_2 concentration exhibit the same behaviour for the investigated experimental conditions (see Fig. 2 and Fig. 3a), whose trend is opposite to that of the O_3 gas density (see Fig. 6), it can be deduced that the peroxone process is not the dominant mechanism forming $^{\bullet}OH$.

$$H_2O_2 \leftrightarrow HO_2^- + H^+ \tag{5}$$

$$O_3 + HO_2^- \to HO_2^{\bullet} + O_3^{\bullet-} \tag{6}$$

$$O_3^{\bullet-} + H_2O \to {}^{\bullet}OH + OH^- + O_2 \tag{7}$$

Photolysis of O_3 or H_2O_2 can take place in the case of a treatment at 9 mm of distance, where the plasma plume directly interacted with the liquid. During this direct plasma treatment, O_3 can induce the formation of metastable atomic oxygen, $O(^1D)$, near the liquid surface (see equation 8). $O(^1D)$ can subsequently contribute to the formation of $^{\bullet}OH$ (see equation 9). The photolysis of H_2O_2 (see equation 10) can also result in the enhancement of the $^{\bullet}OH$ concentration in the liquid phase.

$$O_3 + h\nu \to O_2 + O(^1D) \tag{8}$$

$$O(^1D) + H_2O \to 2\ {}^{\bullet}OH \tag{9}$$

$$H_2O_2 + h\nu \to 2\ {}^{\bullet}OH \tag{10}$$

From the products of reactions 8, 9, and 10, only $O(^1D)$ could form the TEMPD adduct during direct plasma treatment. The peroxone process (see equations 5 to 7) as well as the photolysis of O_3 and/or H_2O_2 (see equations 8 to 10) ends in the formation of $^{\bullet}OH$ and/or $HO_2^{\bullet}/O_2^{\bullet-}$. As these species concentration decrease with increasing O_2 content in the feed gas whereas the TEMPD adduct concentration increases, the reactions are assumed to have minor relevance in the system.

The comparison between the behaviour as a function of the measurement distance of the density of the plasma generated species in the gas phase and of the concentration of the reactive species in the liquid phase helps to identify the species responsible for the formation of the TEMPD-HCl adduct. The curtain gas composition which yielded the highest concentration of ROS in the liquid phase was different for the different plasma treatment distances. In fact, while for the 9 mm distance treatments (direct plasma treatments), the pure N_2 curtain yielded the highest concentration of the spin probe adducts, for longer distances (≥100 mm, indirect plasma treatment), the highest concentrations of the spin probe adducts were always obtained in the air-like surrounding. It should be noted that the concentrations of the reactive species in the liquid phase determined after direct (9 mm) and indirect (≥100 mm) plasma treatments are not directly comparable, as different treatment times were used. Actually, in order to enhance the signal-to-noise ratio in the EPR measurements, the treatment time was extended from 180 s for the 9 mm treatment gap to 600 s for the distances longer than 100 mm.

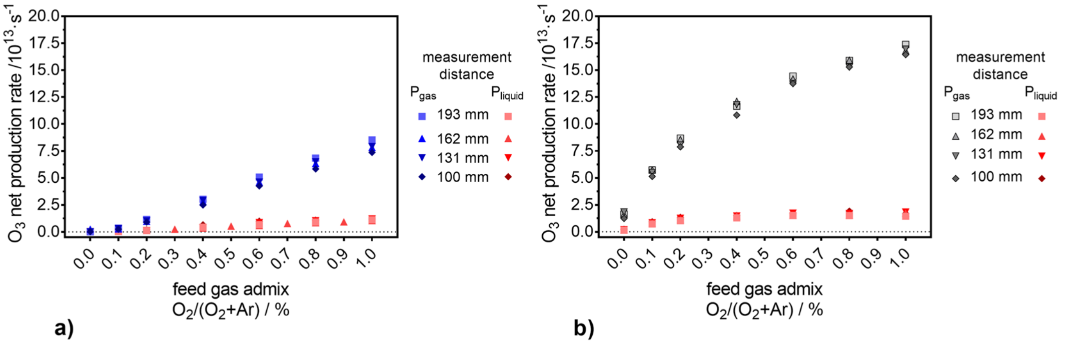

Figure 7. Comparison of the O_3 net production rate in the gas and liquid phases. The net production rates in both phases are determined as a function of the O_2 content in the feed gas under a pure N_2 (**a**) and an air-like (**b**) environment, for different measurement distances.

The photolysis of O_3 or H_2O_2 can also take place for treatment distances longer than 100 mm, as the necessary photon energy for O_3 and H_2O_2 decomposition requires wavelengths of $\lambda < 280$ nm and $\lambda < 300$ nm, respectively[67]. Radiation below 200 nm does not reach the liquid in the investigated distances, as it is almost immediately absorbed in air. The bent shape of the indirect treatment setup also reduces considerably the incident light. Therefore, the decomposition of H_2O_2 and O_3 by light absorption is assumed to be negligible in the indirect treatments (but it can be relevant in the direct treatments).

For all indirect treatments, the trends of the gas phase density of $O_2(a^1\Delta_g)$ are different from those observed for the concentration of TEMPD-HCl in the liquid phase (compare Fig. 4 and Fig. 5). Moreover, the $O_2(a^1\Delta_g)$ gas phase density exhibits a strong dependency on the distance between the plasma jet's nozzle and the point of measurement, while this behaviour was not observed for the TEMPD-HCl adduct formation in the liquid. Additionally, while the use of a pure N_2 curtain gas yielded the highest $O_2(a^1\Delta_g)$ gas phase densities, the highest spin probe adduct concentrations were obtained with an air-like curtain. Finally, in the latter environment, while the TEMPD-HCl adduct concentration depends on the O_2 content in the feed gas, the gas phase $O_2(a^1\Delta_g)$ density does not seem to be influenced by the O_2 admixture into the carrier gas. Thus, it can be concluded that a solvation of gaseous $O_2(a^1\Delta_g)$ cannot be responsible for the measured TEMPD-HCl adducts. $^\bullet$O is another potential reactant with TEMPD-HCl. However, $^\bullet$O is only present in the plasma plume and vanishes directly after leaving it, according to a model of this plasma source[9]. Therefore, for long distance indirect treatments TEMPD-HCl, adducts cannot be linked to $^\bullet$O. Hence, the TEMPD-HCl adduct formation can be attributed to the solvation of gaseous O_3. In fact, the O_3 densities in the gas phase matched remarkably well the TEMPD-HCl adduct concentrations in the liquid phase, as both followed the same trends as a function of the O_2 content in the feed gas for both gas environments, and showed higher amounts for the air-like curtain gas composition and no strict distance dependency (compare Fig. 4 and Fig. 6). For a better comparison, the net production rates of O_3 in the gas phase and the TEMPD adduct in the liquid phase were calculated. For the gas phase, the net production rate was determined via equation (11):

$$P_g(O_3) = n(O_3) \cdot 4.9 \cdot 10^{-4} \cdot (\Phi_1 + \Phi_2) \cdot 16.67\ \mathrm{cm}^3 \cdot \mathrm{s}^{-1} \cdot \mathrm{slm}^{-1}, \qquad (11)$$

where the gas phase O_3 density ($n(O_3)$) is given in particles per cm^3, the factor $4.9 \cdot 10^{-4}$ is the dimensionless Henry constant of O_3[69], Φ_1 and Φ_2 are the feed gas (3 slm) and the curtain gas (5 slm) flow rates, respectively, and 16.67 is the conversion factor of standard litre per minute into the SI unit $cm^{-3}s^{-1}$. The net production rate of O_3 in the liquid phase was calculated via equation (12):

$$P_l(O_3) = c(O_3) \cdot V_L \cdot N_A / t_{treatment}, \qquad (12)$$

where $c(O_3)$ is the concentration of the TEMPD-HCl spin adduct in the liquid, V_L the liquid volume (5 mL), N_A the Avogadro constant and $t_{treatment}$ the treatment time. Both net production rates are compared in Fig. 7a for the pure N_2 curtain gas condition. The agreement between the gas and liquid net production rates is good, albeit a slightly increasing difference towards higher O_2 amounts in the feed gas. This offset is due to the Henry constant of O_3, which is relatively low – $1.2 \cdot 10^{-7}$ M/Pa[69]. Hence, a (local) saturation of the O_3 concentration in the liquid phase is reached relatively fast.

For an air-like surrounding, the net production rates were higher compared to the pure N_2 gas curtain (compare Fig. 7a and Fig. 7b). This is especially the case for the O_3 net production rate in the gas phase, where the values were more than twice as high (see Fig. 7b), and did not reach a plateau. However, the net production rate of the O_3 deposited in the liquid showed a saturation plateau around $1.5 \cdot 10^{17}\ s^{-1}$. Hence, for an air-like atmosphere, the trends of both net production rates curves did not agree completely; again, this is caused by the limited solvation of O_3 in aqueous solutions.

It can be concluded that the similarity of the net production rates in both phases allows the identification of the oxygen species responsible for the formation of the TEMPD-HCl adducts in the liquid upon indirect plasma treatments. In fact, for treatment distanceslonger than 100 mm, the spin probe adduct is formed by reaction with O_3. However, for direct plasma treatments, when the plasma plume interacts directly with the liquid, such statement cannot be given, since the detection of at least one of the potential reactants with TEMPD-HCl, namely $O_2(a^1\Delta_g)$, is not experimentally feasible at this distance.

$$O_3 + OH^- \rightarrow HO_2^\bullet + O_2^{\bullet -} \tag{13}$$

$$HO_2^\bullet \leftrightarrow H^+ + O_2^{\bullet -} \quad pK_a = 4.8 \tag{14}$$

$$O_3 + OH^- \rightarrow HO_2^- + O_2 \tag{15}$$

$$H_2O_2 \leftrightarrow H^+ + HO_2^- \quad pK_a = 11.6 \tag{16}$$

$$O_3 + OH^- \rightarrow O_3^{\bullet -} + {}^\bullet OH \tag{17}$$

$$O_3 + O_2^{\bullet -} \rightarrow O_3^{\bullet -} + O_2 \tag{18}$$

$$O_3^{\bullet -} + H_2O \rightarrow {}^\bullet OH + OH^- + O_2 \tag{19}$$

$$O_3 + Cl^- \leftrightarrow O_3^- + Cl \quad \approx 70\% \tag{20}$$

$$O_3 + Cl^- \rightarrow OCl^- + O_2 \quad \approx 30\% \tag{21}$$

The O_3 decomposes via ions, hydroxide (OH^-)[70], chloride (Cl^-)[71], or $O_2^{\bullet -}$ [70] in aqueous or saline solutions[71] (see reactions 13 to 21). For instance, $^\bullet OH$ (see equations 17 and 19) or even OCl^- can be formed by interaction of O_3 with chlorite ions (see equations 20 and 21). However, the formation of OCl^- due to reaction 21 is subordinated, as only 30% of the formed product yields OCl^- [71]. It should be noted, though, that, in other publications[72,73], especially in Liu *et al.*[74], this pathway is mentioned as the main formation pathway of OCl^-. Hence, dissolved O_3, as a gaseous precursor of other oxidizing molecules in a plasma treated liquid, is of great relevance for plasma liquid chemistry in the context of biomedical applications of plasmas, especially for jet-like plasmas where a strong stirring of the liquid occurs.

Conclusion

The present study has yielded relevant insight for the medical application of plasma treatment. By varying the treatment distance, the composition, and, therefore, the oxidizing potential of the cocktail of generated species can be modulated. It was shown that during a direct plasma treatment, the role of $^\bullet O$ cannot be excluded, but in the case of longer treatment distances, or treatments with just the plasma gas exhaust, O_3 is the main active component. $O_2(a^1\Delta_g)$ is also formed during plasma treatment. The $O_2(a^1\Delta_g)$ gas density is an order of magnitude lower than the O_3 gas density. Moreover, according to their respective Henry constants, also the solubility of $O_2(a^1\Delta_g)$ is slightly lower. Thus, it was elucidated that, for the investigated experimental conditions, O_3 is the dominating species, being originated in the gas phase and subsequently transported to the liquid phase by solvation. By correlating the behaviour of different ROS, several reaction pathways were excluded or their importance for the proceeding reactions was weighted.

Methods

Plasma source.

In this study, an argon atmospheric pressure plasma jet was investigated. This plasma source was a commercial plasma jet called kinpen09 (neoplas GmbH, Greifswald, Germany). It consists of a ceramic capillary (1.6 mm in diameter) with a centred rod electrode inside, and a grounded ring electrode close to the end of the capillary. The rod electrode was driven at a frequency of around 1 MHz. The dissipated power in the plasma was of 1.1 W[75]. The working gas flow was set to 3 standard litres per minute (slm); the carrier gas was argon with up to 1% of molecular oxygen admixture (argon N50, oxygen N48, Air Liquide, Paris, France). A controlled environment during the plasma treatment was provided by the application of a curtain gas device (see yellow-shaded areas in Fig. 8) fed with molecular nitrogen or synthetic air as gases (gas inlet indicated by yellow arrows), at a total gas flow rate of 5 slm (oxygen N48, nitrogen N50, Air Liquide, Paris, France). A detailed study of the effect of the curtain gas on the plasma jet can be found in previous publications[58,60].

The liquid treatment took place in Petri dishes of 60 mm in diameter filled with a liquid volume of 5 mL of Dulbecco's phosphate buffered saline solution (DPBS). The direct treatment was performed for a distance of 9 mm between the liquid surface and the end of the capillary, which is also called the plasma jet's nozzle (see Fig. 8a), for 180 s.

Gas phase diagnostics.

For the gas phase diagnostics, a modified setup had to be used. This setup is schematically shown in Fig. 8b). To avoid scattered light or direct light from the plasma interfering with the measurements, the plasma jet cannot be connected directly to the measurement cell. As so, the plasma jet, including the curtain gas device, was enclosed in a glass capsule connected to the measurement cell through a bent glass tube. The measurement cell has an outlet for the exhaust, which was used to treat the liquid.

In order to study the role of $O_2(a^1\Delta_g)$ and O_3, the distance between the plasma jet's nozzle and the measurement cell was varied by adding, in-between the measurement cell (blue-shaded area in Fig. 8b) and the bent glass tube, glass connectors (green-shaded area in Fig. 8b) with different lengths (up to 92 mm, as indicated by the

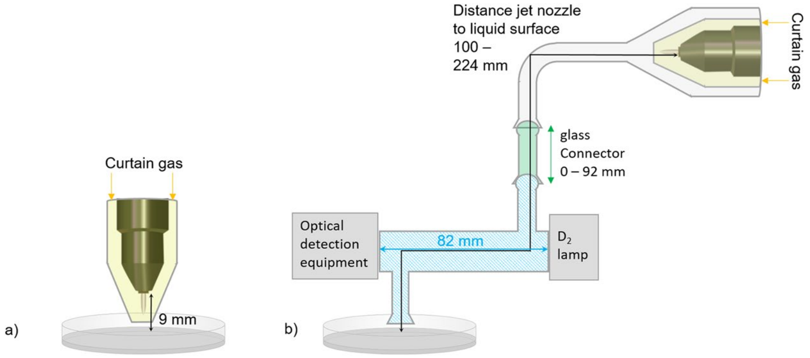

Figure 8. Experimental setup of the plasma treatment of liquid samples under controlled environment. Direct plasma treatment (**a**) was performed for a 9 mm distance between the plasma jet's nozzle and the liquid surface. In (**b**), the modified setup for the investigation of $O_2(a^1\Delta_g)$ and O_3 is shown. To avoid direct or scattered light from the plasma interfering with the measurement of $O_2(a^1\Delta_g)$ and O_3, the kinpen09 with its curtain gas device (yellow-shaded area, gas inlet indicated by the yellow arrows) was enclosed in a glass capsule connected to the measurement cell through a bent glass tube. Glass connectors (green-shaded area) with different lengths (up to 92 mm, as indicated by the green double-headed arrow) were added in-between the measurement cell and the bent glass tube. The optical path length of the measurement cell (blue-shaded area) was 82 mm, as indicated by the blue double-headed arrow. The optical detection equipment used for measuring $O_2(a^1\Delta_g)$ and O_3 (InGaAs detector + filter and UV/VIS spectrometer + filter + convex lens, respectively) was placed at one end of the measurement cell. For the indirect plasma treatment (**b**), the distance between the plasma jet's nozzle and the liquid surface varied in the range 100–224 mm (as indicated by the black double-headed arrow).

green double-headed arrow in Fig. 8). The investigated distances between the end of the capillary of the plasma jet and the point of measurement of $O_2(a^1\Delta_g)$ and O_3 were 100 mm, 131 mm, 162 mm, 193 mm, and 224 mm (as indicated by the black double-headed arrow in Fig. 8).

The $O_2(a^1\Delta_g)$ density was measured via optical emission spectroscopy in the near infrared (NIR) region at 1270 nm, by using an InGaAs detector (Judson model J22D-M204) and a 19 nm band pass interference filter (Andover 200FC39-25/1270)[54]. The signal collected by the detector was amplified and monitored with an oscilloscope (Tektronix DPO 2024B). The detector was placed behind a calibrated detection cell (blue-shaded area in Fig. 8b) equipped with quartz windows. This cell has a path length of 82 mm (indicated by the blue double-headed arrow in Fig. 8b)[76]. The used system has a $O_2(a^1\Delta_g)$ density detection limit of $4\ 10^{13}\,\mathrm{cm}^{-3}$.

The O_3 density was measured by ultraviolet absorption spectroscopy at 254 nm. A deuterium lamp with a broadband spectrum between 180 and 400 nm was used as UV source (OceanOptics, DH-2000-BAL). The UV radiation was guided through the same measurement cell that was used for the $O_2(a^1\Delta_g)$ density measurements. For the O_3 absorption measurements, this cell was used as an absorption cell (path length of 82 mm) and the intensity of the transmitted radiation was measured by an UV/VIS spectrometer (avantes) with a filter (254 nm) and a convex lens (f = 35) placed in front of it. For deduction of the O_3 density, the ratio of the intensity (I) transmitted when the plasma was ignited and the intensity (I_0) transmitted when the plasma was not ignited was calculated. The O_3 density was calculated from the Beer's law (equation 22) with the cross section $\sigma = 1.14\cdot 10^{-17}$ cm^2[77] and the path length L = 82 mm. The O_3 concentration is assumed to be constant across the absorption path length.

$$n(O_3) = \frac{\ln(\ I_0/I)}{\sigma\ \cdot L} \tag{22}$$

Liquid phase analytic. For the liquid analysis, the pH values were measured electrochemically via a pH meter (SevenMulti™ S47, Mettler-Toledo International Inc., Columbus, OH, USA) equipped with a pH electrode (InLab® Micro, Mettler-Toledo International Inc., Columbus, OH, USA).

The hydrogen peroxide (H_2O_2) concentration was determined by commercially available test stripes (Merckoquant 110011, Merck) enhanced with a camera read out (digital microscope camera with 1.3 million pixels, zoom factor 10 to 200x, Conrad, Germany). The camera was in a dark box with defined constant light conditions in order to precisely analyse the colour of the sensor part of test stripes by determination of the red-, green- and blue-values[17]. Prior to each experiment, a calibration was conducted, where the related colour values of hydrogen peroxide concentrations in the range of 0–180 µM (0–6 mg/L) were determined.

The electron paramagnetic resonance (EPR) spectroscope used in this work is an X-band (equals to microwave frequency of 9.87 GHz) EPR (EMXmicro, Bruker BioSpin GmbH, Rheinstetten, Germany) with the resonator ER 4119HS (Bruker BioSpin GmbH, Rheinstetten, Germany). The applied instrument's parameters of the EPR spectroscope were the same for all measurements: modulation frequency of 100 kHz, modulation amplitude of 0.1 mT, microwave power of 5.024 mW, receiver gain of 30 dB, time constant of 0.01 ms. The magnetic field scan was adjusted according to the sample measured; in this work, a range of 10 mT was used.

The measurement procedure followed always the same protocol, including performing measurements in triplicates for each sample. Prior to a measurement, the spin trap solution was prepared and 50 µL of the untreated solution were taken as control. All samples, treated and untreated, were pipetted into a borosilicate glass tube (125 mm length, 0.8525 mm inner diameter) for the measurement. From the plasma treatment to the measurement, a few minutes were needed due to handling reasons. This delay time was always fixed to four minutes. The spectrum of the untreated control was subtracted from the measured EPR signal. The evaluation of the EPR spectra was performed by assistance of the evaluation software (Xenon software with Xenon Spin Counting module, Bruker BioSpin, Rheinstetten, Germany). As the spectroscope was calibrated, absolute spin numbers could be gained.

In the presented work, 5-tert-Butoxycarbonyl-5-methyl-1-pyrroline-N-oxide (BMPO, 2 mM) was used as a spin trap for $^{\bullet}OH$ and $O_2^{\bullet-}$ radicals, and 2,2,6,6-tetramethyl-4- piperidone hydrochloride (TEMPD-HCl, 100 mM) was used as a spin probe for $^{\bullet}O$, $O_2(a^1\Delta_g)$, or O_3. The used BMPO concentration was chosen based on previous studies[19] using the exactly same plasma source, where higher concentrations yielded similar adduct concentrations in the µM range. Therefore, the chosen concentration of 2 mM is high enough to trap all detectable radicals. The TEMPD-HCl concentration used in the study was based on literature[78]; furthermore, the used concentrations were far higher than the detected adduct concentration, so that the spin trap was offered in excess.

Data availability. The datasets generated during and/or analysed during the current study are available from the corresponding author on reasonable request.

References

1. Hasse, S. *et al.* Induction of proliferation of basal epidermal keratinocytes by cold atmospheric-pressure plasma. *Clin Exp Dermatol* **41**, 202–209, https://doi.org/10.1111/ced.12735 (2016).
2. Daeschlein, G. *et al. In Vitro* Susceptibility of Multidrug Resistant Skin and Wound Pathogens Against Low Temperature Atmospheric Pressure Plasma Jet (APPJ) and Dielectric Barrier Discharge Plasma (DBD). *Plasma Process Polym* **11**, 175–183, https://doi.org/10.1002/ppap.201300070 (2014).
3. Isbary, G. *et al.* Reasons why we need cold atmospheric plasmas in bacteria related diseases in medicine. *Plasma Medicine*, https://doi.org/10.1615/PlasmaMed.2014006273 (2014).
4. Weltmann, K. D. & von Woedtke, T. Plasma medicine-current state of research and medical application. *Plasma Physics and Controlled Fusion* **59**, 014031, https://doi.org/10.1088/0741-3335/59/1/014031 (2017).
5. Emmert, S. *et al.* Atmospheric pressure plasma in dermatology: Ulcus treatment and much more. *Clinical Plasma Medicine* **1**, 24–29, https://doi.org/10.1016/j.cpme.2012.11.002 (2013).
6. Lu, X. *et al.* Reactive species in non-equilibrium atmospheric-pressure plasmas: Generation, transport, and biological effects. *Physics Reports* **630**, 1–84, https://doi.org/10.1016/j.physrep.2016.03.003 (2016).
7. Schmidt, A., von Woedtke, T. & Bekeschus, S. Periodic Exposure of Keratinocytes to Cold Physical Plasma: An *In Vitro* Model for Redox-Related Diseases of the Skin. *Oxid Med Cell Longev* **2016**, 9816072, https://doi.org/10.1155/2016/9816072 (2016).
8. Schmidt-Bleker, A., Bansemer, R., Reuter, S. & Weltmann, K.-D. How to produce an NOx- instead of Ox-based chemistry with a cold atmospheric plasma jet. *Plasma Process Polym* **13**, 1120–1127, https://doi.org/10.1002/ppap.201600062 (2016).
9. Schmidt-Bleker, A., Winter, J., Bösel, A., Reuter, S. & Weltmann, K.-D. On the plasma chemistry of a cold atmospheric argon plasma jet with shielding gas device. *Plasma Sources Science and Technology* **25**, 015005 (2015).
10. Jablonowski, H. & von Woedtke, T. Research on plasma medicine-relevant plasma–liquid interaction: What happened in the past five years? *Clinical Plasma Medicine* **3**, 42–52, https://doi.org/10.1016/j.cpme.2015.11.003 (2015).
11. Wende, K. *et al.* Identification of the biologically active liquid chemistry induced by a nonthermal atmospheric pressure plasma jet. *Biointerphases* **10**, 029518, https://doi.org/10.1116/1.4919710 (2015).
12. Bruggeman, P. J. *et al.* Plasma-liquid interactions: a review and roadmap. *Plasma Sources Sci T* **25**, 053002, https://doi.org/10.1088/0963-0252/25/5/053002 (2016).
13. Jablonowski, H. *et al.* Plasma Jet (V) UV-Radiation Impact on Biologically Relevant Liquids and Cell Suspension. *Bulletin of the American Physical Society* **59** (2014).
14. Attri, P. *et al.* Generation mechanism of hydroxyl radical species and its lifetime prediction during the plasma-initiated ultraviolet (UV) photolysis. *Sci Rep* **5**, 9332, https://doi.org/10.1038/srep09332 (2015).
15. Winter, J. *et al.* Tracking plasma generated H_2O_2 from gas into liquid phase and revealing its dominant impact on human skin cells. *J Phys D Appl Phys* **47**, 285401, https://doi.org/10.1088/0022-3727/47/28/285401 (2014).
16. Lukes, P., Dolezalova, E., Sisrova, I. & Clupek, M. Aqueous-phase chemistry and bactericidal effects from an air discharge plasma in contact with water: evidence for the formation of peroxynitrite through a pseudo-second-order post-discharge reaction of H_2O_2 and HNO_2. *Plasma Sources Science and Technology* **23**, 015019, https://doi.org/10.1088/0963-0252/23/1/015019 (2014).
17. Winter, J. *et al.* Feed gas humidity: a vital parameter affecting a cold atmospheric-pressure plasma jet and plasma-treated human skin cells. *J Phys D Appl Phys* **46**, 295401, https://doi.org/10.1088/0022-3727/46/29/295401 (2013).
18. Gorbanev, Y., O'Connell, D. & Chechik, V. Non-Thermal Plasma in Contact with Water: The Origin of Species. *Chemistry* **22**, 3496–3505, https://doi.org/10.1002/chem.201503771 (2016).
19. Tresp, H., Hammer, M. U., Winter, J., Weltmann, K. D. & Reuter, S. Quantitative detection of plasma-generated radicals in liquids by electron paramagnetic resonance spectroscopy. *J Phys D Appl Phys* **46**, 435401, https://doi.org/10.1088/0022-3727/46/43/435401 (2013).
20. Jablonowski, H. *et al.* Impact of plasma jet vacuum ultraviolet radiation on reactive oxygen species generation in bio-relevant liquids. *Physics of Plasmas* **22**, 122008, https://doi.org/10.1063/1.4934989 (2015).
21. Gorbanev, Y., Stehling, N., O'Connell, D. & Chechik, V. Reactions of nitroxide radicals in aqueous solutions exposed to non-thermal plasma: limitations of spin trapping of the plasma induced species. *Plasma Sources Sci T* **25**, 055017, https://doi.org/10.1088/0963-0252/25/5/055017 (2016).
22. Girard, F. *et al.* Formation of reactive nitrogen species including peroxynitrite in physiological buffer exposed to cold atmospheric plasma. *Rsc Advances* **6**, 78457–78467, https://doi.org/10.1039/c6ra12791f (2016).
23. Norberg, S. A., Tian, W., Johnsen, E. & Kushner, M. J. Atmospheric pressure plasma jets interacting with liquid covered tissue: touching and not-touching the liquid. *J Phys D Appl Phys* **47**, 475203, https://doi.org/10.1088/0022-3727/47/47/475203 (2014).
24. Tian, W. & Kushner, M. J. Atmospheric pressure dielectric barrier discharges interacting with liquid covered tissue. *J Phys D Appl Phys* **47**, 165201, https://doi.org/10.1088/0022-3727/47/16/165201 (2014).
25. van Gils, C. A. J., Hofmann, S., Boekema, B. K. H. L., Brandenburg, R. & Bruggeman, P. J. Mechanisms of bacterial inactivation in the liquid phase induced by a remote RF cold atmospheric pressure plasma jet. *Journal of Physics D: Applied Physics* **46**, 175203, https://doi.org/10.1088/0022-3727/46/17/175203 (2013).

26. Chen, C. *et al.* A Model of Plasma-Biofilm and Plasma-Tissue Interactions at Ambient Pressure. *Plasma Chemistry and Plasma Processing* **34**, 403–441, https://doi.org/10.1007/s11090-014-9545-1 (2014).
27. Alexander, D. L., David, B. G. & Steven, C. S. Fully coupled simulation of the plasma liquid interface and interfacial coefficient effects. *Journal of Physics D: Applied Physics* **49**, 235204 (2016).
28. Amanda, M. L. & Mark, J. K. Air plasma treatment of liquid covered tissue: long timescale chemistry. *Journal of Physics D: Applied Physics* **49**, 425204 (2016).
29. Bekeschus, S. *et al.* Cold physical plasma selects for specific T helper cell subsets with distinct cells surface markers in a caspase-dependent and NF-κB-independent manner. *Plasma Process Polym* **13**, 1144–1150, https://doi.org/10.1002/ppap.201600080 (2016).
30. Schmidt, A. *et al.* Redox-regulation of activator protein 1 family members in blood cancer cell lines exposed to cold physical plasma-treated medium. *Plasma Process Polym* **13**, 1179–1188, https://doi.org/10.1002/ppap.201600090 (2016).
31. von Woedtke, T. *et al.* In *20th Int. Symp. on Plasma Chemistry (ISPC-20)* (2011).
32. von Woedtke, T., Metelmann, H. R. & Weltmann, K. D. Clinical Plasma Medicine: State and Perspectives ofin VivoApplication of Cold Atmospheric Plasma. *Contributions to Plasma Physics* **54**, 104–117, https://doi.org/10.1002/ctpp.201310068 (2014).
33. Chen, Z. T., Lin, L., Cheng, X. Q., Gjika, E. & Keidar, M. Effects of cold atmospheric plasma generated in deionized water in cell cancer therapy. *Plasma Process Polym* **13**, 1151–1156, https://doi.org/10.1002/ppap.201600086 (2016).
34. Collet, G. *et al.* Plasma jet-induced tissue oxygenation: potentialities for new therapeutic strategies. *Plasma Sources Sci T* **23**, 012005, https://doi.org/10.1088/0963-0252/23/1/012005 (2014).
35. Nasruddin *et al.* A Simple Technique to Improve Contractile Effect of Cold Plasma Jet on Acute Mouse Wound by Dropping Water. *Plasma Process Polym* **12**, 1128–1138, https://doi.org/10.1002/ppap.201400236 (2015).
36. Tanaka, H. *et al.* Non-thermal atmospheric pressure plasma activates lactate in Ringer's solution for anti-tumor effects. *Sci Rep* **6**, 36282, https://doi.org/10.1038/srep36282 (2016).
37. Bekeschus, S. *et al.* Oxygen atoms are critical in rendering THP-1 leukaemia cells susceptible to cold physical plasma-induced apoptosis. *Sci Rep* **7**, 2791, https://doi.org/10.1038/s41598-017-03131-y (2017).
38. Vasilets, V. N., Shekhter, A. B., Guller, A. E. & Pekshev, A. V. Air plasma-generated nitric oxide in treatment of skin scars and articular musculoskeletal disorders: Preliminary review of observations. *Clinical Plasma Medicine* **3**, 32–39, https://doi.org/10.1016/j.cpme.2015.05.001 (2015).
39. Oehmigen, K. *et al.* Estimation of Possible Mechanisms of Escherichia coli Inactivation by Plasma Treated Sodium Chloride Solution. *Plasma Process Polym* **8**, 904–913, https://doi.org/10.1002/ppap.201000099 (2011).
40. Winter, J. *et al.* Aspects of UV-absorption spectroscopy on ozone in effluents of plasma jets operated in air. *J Phys D Appl Phys* **45**, 385201, https://doi.org/10.1088/0022-3727/45/38/385201 (2012).
41. Santos Sousa, J. *et al.* Cold atmospheric pressure plasma jets as sources of singlet delta oxygen for biomedical applications. *J Appl Phys* **109**, 123302, https://doi.org/10.1063/1.3601347 (2011).
42. Glaze, W. H., Kang, J. W. & Chapin, D. H. The Chemistry of Water-Treatment Processes Involving Ozone, Hydrogen-Peroxide and Ultraviolet-Radiation. *Ozone-Sci Eng* **9**, 335–352, https://doi.org/10.1080/01919518708552148 (1987).
43. Hoigne, J. & Bader, H. Ozonation of Water - Role of Hydroxyl Radicals as Oxidizing Intermediates. *Science* **190**, 782–784, https://doi.org/10.1126/science.190.4216.782 (1975).
44. Hoigné, J. The Chemistry of Ozone in Water. 121–141, https://doi.org/10.1007/978-1-4684-8556-1_11 (1988).
45. Pan, G., Chen, C.-L., Chang, H.-M. & Gratzl, J. Studies on ozone bleaching. I. The effect of pH, temperature, buffer systems and heavy metal-ions on stability of ozone in aqueous solution. *Journal of wood chemistry and technology* **4**, 367–387 (1984).
46. Aruoma, O. I. Free radicals, oxidative stress, and antioxidants in human health and disease. *J Am Oil Chem Soc* **75**, 199–212, https://doi.org/10.1007/s11746-998-0032-9 (1998).
47. McClurkin, J. & Maier, D. Half-life time of ozone as a function of air conditions and movement. *Julius-Kühn-Archiv*, **381**, https://doi.org/10.5073/jka.2010.425.167.326 (2010).
48. Wilkinson, F., Helman, W. P. & Ross, A. B. Rate Constants for the Decay and Reactions of the Lowest Electronically Excited Singlet-State of Molecular-Oxygen in Solution - an Expanded and Revised Compilation. *Journal of Physical and Chemical Reference Data* **24**, 663–1021, https://doi.org/10.1063/1.555965 (1995).
49. Halliwell, B. & Gutteridge, J. M. Oxygen toxicity, oxygen radicals, transition metals and disease. *Biochem J* **219**, 1–14, https://doi.org/10.1042/bj2190001 (1984).
50. Halliwell, B. & Gutteridge, J. M. C. *Free Radicals in Biology and Medicine*. (Oxford University Press, 2007).
51. Riethmüller, M., Burger, N. & Bauer, G. Singlet oxygen treatment of tumor cells triggers extracellular singlet oxygen generation, catalase inactivation and reactivation of intercellular apoptosis-inducing signaling. *Redox Biology* **6**, 157–168, https://doi.org/10.1016/j.redox.2015.07.006 (2015).
52. Nayak, G., Santos Sousa, J. & Bruggeman, P. J. Singlet delta oxygen production in a 2D micro-discharge array in air: effect of gas residence time and discharge power. *Journal of Physics D: Applied Physics* **50**, 105205, https://doi.org/10.1088/1361-6463/aa5764 (2017).
53. Santos Sousa, J., Bauville, G., Lacour, B., Puech, V. & Touzeau, M. Atmospheric pressure generation of O-2(a(1)Delta(g)) by microplasmas. *European Physical Journal-Applied Physics* **47**, https://doi.org/10.1051/epjap/2009103 (2009).
54. Santos Sousa, J. *et al.* O(2)(a(1)Delta(g)) production at atmospheric pressure by microdischarge. *Appl Phys Lett* **93**, https://doi.org/10.1063/1.2957032 (2008).
55. Santos Sousa, J., Bauville, G. & Puech, V. Arrays of microplasmas for the controlled production of tunable high fluxes of reactive oxygen species at atmospheric pressure. *Plasma Sources Sci T* **22**, 035012, https://doi.org/10.1088/0963-0252/22/3/035012 (2013).
56. Reuter, S. *et al.* Detection of ozone in a MHz argon plasma bullet jet. *Plasma Sources Sci T* **21**, 034015, https://doi.org/10.1088/0963-0252/21/3/034015 (2012).
57. Schmidt-Bleker, A. *et al.* Propagation mechanisms of guided streamers in plasma jets: the influence of electronegativity of the surrounding gas. *Plasma Sources Sci T* **24**, 035022, https://doi.org/10.1088/0963-0252/24/3/035022 (2015).
58. Reuter, S. *et al.* Controlling the Ambient Air Affected Reactive Species Composition in the Effluent of an Argon Plasma Jet. *Ieee T Plasma Sci* **40**, 2788–2794, https://doi.org/10.1109/Tps.2012.2204280 (2012).
59. Jablonowski, H. *et al.* Plasma jet's shielding gas impact on bacterial inactivation. *Biointerphases* **10**, 029506, https://doi.org/10.1116/1.4916533 (2015).
60. Reuter, S. *et al.* From RONS to ROS: Tailoring Plasma Jet Treatment of SkinCells. *Ieee T Plasma Sci* **40**, 2986–2993, https://doi.org/10.1109/Tps.2012.2207130 (2012).
61. Tresp, H., Hammer, M. U., Weltmann, K.-D. & Reuter, S. Effects of Atmosphere Composition and Liquid Type on Plasma-Generated Reactive Species in Biologically Relevant Solutions. *Plasma Medicine* **3**, 45–55, https://doi.org/10.1615/PlasmaMed.2014009711 (2013).
62. Bauer, G. The Antitumor Effect of Singlet Oxygen. *Anticancer Res* **36**, 5649–5663, https://doi.org/10.21873/anticanres.11148 (2016).
63. Takamatsu, T. *et al.* Microbial Inactivation in the Liquid Phase Induced by Multigas Plasma Jet. *PloS one* **10**, e0132381, https://doi.org/10.1371/journal.pone.0132381 (2015).
64. Tarr, M. & Valenzeno, D. P. Singlet oxygen: the relevance of extracellular production mechanisms to oxidative stress *in vivo*. *Photochem Photobiol Sci* **2**, 355–361, https://doi.org/10.1039/b211778a (2003).
65. Liu, D. X. *et al.* Aqueous reactive species induced by a surface air discharge: Heterogeneous mass transfer and liquid chemistry pathways. *Sci Rep* **6**, 23737, https://doi.org/10.1038/srep23737 (2016).

66. Gaens, W. V. *et al*. Numerical analysis of the effect of nitrogen and oxygen admixtures on the chemistry of an argon plasma jet operating at atmospheric pressure. *New J Phys* **17**, 033003, https://doi.org/10.1088/1367-2630/17/3/033003 (2015).
67. Parvulescu, V. I., Magureanu, M. & Lukes, P. *Plasma Chemistry and Catalysis in Gases and Liquids*. (Wiley, 2013).
68. Merenyi, G., Lind, J., Naumov, S. & Sonntag, C. Reaction of ozone with hydrogen peroxide (peroxone process): a revision of current mechanistic concepts based on thermokinetic and quantum-chemical considerations. *Environ Sci Technol* **44**, 3505–3507, https://doi.org/10.1021/es100277d (2010).
69. Sander, R. Compilation of Henry's law constants (version 4.0) for water as solvent. *Atmospheric Chemistry and Physics* **15**, 4399–4981, https://doi.org/10.5194/acp-15-4399-2015 (2015).
70. Staehelin, J. & Hoigne, J. Decomposition of Ozone in Water - Rate of Initiation by Hydroxide Ions and Hydrogen-Peroxide. *Environmental Science & Technology* **16**, 676–681, https://doi.org/10.1021/es00104a009 (1982).
71. Razumovskii, S. D., Konstantinova, M. L., Grinevich, T. V., Korovina, G. V. & Zaitsev, V. Y. Mechanism and kinetics of the reaction of ozone with sodium chloride in aqueous solutions. *Kinetics and Catalysis* **51**, 492–496, https://doi.org/10.1134/S0023158410040051 (2010).
72. Knipping, E. & Dabdub, D. Modeling Cl~ 2 formation from aqueous NaCl particles: Evidence for interfacial reactions and importance of Cl~ 2 decomposition in alkaline solution. *Journal of geophysical research-all series-* **107**, ACH 8–ACH 8, https://doi.org/10.1029/2001JD000867 (2002).
73. Rao, B., Anderson, T. A., Redder, A. & Jackson, W. A. Perchlorate formation by ozone oxidation of aqueous chlorine/oxy-chlorine species: role of ClxOy radicals. *Environ Sci Technol* **44**, 2961–2967, https://doi.org/10.1021/es903065f (2010).
74. Liu, Z. C. *et al*. Chemical Kinetics and Reactive Species in Normal Saline Activated by a Surface Air Discharge. *Plasma Process Polym* **14**, n/a-n/a, https://doi.org/10.1002/ppap.201600113 (2017).
75. Schmidt-Bleker, A., Reuter, S. & Weltmann, K. D. Quantitative schlieren diagnostics for the determination of ambient species density, gas temperature and calorimetric power of cold atmospheric plasma jets. *J Phys D Appl Phys* **48**, 175202, https://doi.org/10.1088/0022-3727/48/17/175202 (2015).
76. Santos Sousa, J. & Puech, V. Diagnostics of reactive oxygen species produced by microplasmas. *J Phys D Appl Phys* **46**, 464005, https://doi.org/10.1088/0022-3727/46/46/464005 (2013).
77. Orphal, J. A critical review of the absorption cross-sections of O3 and NO2 in the ultraviolet and visible. *Journal of Photochemistry and Photobiology A: Chemistry* **157**, 185–209, https://doi.org/10.1016/s1010-6030(03)00061-3 (2003).
78. Hideg, E. *et al*. Pure forms of the singlet oxygen sensors TEMP and TEMPD do not inhibit Photosystem II. *Biochim Biophys Acta* **1807**, 1658–1661, https://doi.org/10.1016/j.bbabio.2011.09.009 (2011).

Acknowledgements

Authors are grateful to Dr. Jörn Winter, Dr. Ansgar Schmidt-Bleker, Dana Sponholz, Melanie Schulz and Julia Koch for their help. This work was funded by the German Federal Ministry of Education and Research (BMBF) (Grant No. 03Z2DN12 & 03Z22DN12), as well as by the Ministry of Education, Science and Culture of the State of Mecklenburg-Vorpommern (Grant No: AU 15 001).

Author Contributions

H.J., J.S.S. and S.R. conceived and designed the experiments. H.J. performed all liquid analytic experiments as well as the O_3 measurements in the gas phase. J.S.S. and S.R. performed and analysed the $O_2(a^1\Delta_g)$ measurements in the gas phase. K.W. provided assistance with the chemical interpretation. All authors discussed the results. H.J. conceived and wrote the main manuscript and prepared all figures. All authors reviewed the manuscript.

Additional Information

Competing Interests: The authors declare no competing interests.